Multiscale Resolution of Fluidized-Bed Pressure Fluctuations

Gui-Bing Zhao and Yong-Rong Yang
Dept. of Chemical Engineering and Biochemical Engineering, Zhejiang University, Hangzhou 310027, P.R. China

Pressure fluctuation signals measured from four different axial locations in a bubbling bed 0.3 m in diameter and 3 m in height were analyzed using multiple approaches, including wavelet transform, Hurst analysis, multiscale resolution, and time-delay embedding. After examining decomposition residuals using different compact support Daubechies wavelets, the Daubechies second-order wavelet was chosen as an optimal wavelet for decomposing pressure signals. Hurst analysis of the decomposed signals shows that the measured pressure fluctuations can be resolved to three characteristic scales: bifractal mesoscale signals with two distinct Hurst exponents; monofractal micro- and macroscale signals with only one characteristic Hurst exponent. Energy profiles of the three scale components confirm that the measured pressure signals mainly reflect the mesoscale component. Time-delay embedding analysis of three scale signals demonstrates that the microscale dynamics is more complex than the mesoscale dynamics, and the mesoscale dynamics is more complex than the macroscale dynamics. That this result cannot be found solely from Hurst analysis shows the importance of integrating multiple approaches for characterizing the complexity of fluidized systems.

Introduction

Fluidization is an important technology employed in a variety of industrial processes. It plays a major role not only in traditional industries, such as coal combustion, oil refining, and metallurgical processes, but also in the development of emerging technologies, such as materials processing and biotechnology. With increasing demand for sustainable development, its applications in energy, resource recovery, and environment are being explored further. On the other hand, however, fluidization is one of the most complicated unit operations in practice. Its typical particle–fluid two-phase flow patterns exhibit nonlinear and nonequilibrium dynamic characteristics with heterogeneous flow structure. Therefore, its quantitative understanding and practical application constitute a challenge in science and engineering. Further efforts are, therefore, still needed in order to understand its mechanism for realizing quantitative design and optimal operation of fluidized-bed reactors. Fortunately, however, the advance of the interdisciplinary sciences has further stimulated its fundamental research.

The complexity of particle–fluid two-phase flow mainly results from structure heterogeneity and regime multiplicity and their nonlinear behavior (Li et al., 1996). Li and Kwauk (1994) proposed that the complex dynamics of a fluidization system can be reduced to three scales: microscale of discrete individual particles inside either the dense or the dilute phase, mesoscale of cluster size involving interaction between the dilute broth phase and the dense cluster phase, and macroscale, which encompasses the global system of the particle–fluid suspension within its boundaries (see Li et al., 1999, for a review on more details). Therefore, a very complicated fluidization system becomes easy to describe and understand after resolution. And many studies have found that this complexity can be well understood by the multiscale method (Li et al., 1999; Cui et al., 2000; Li, 2000; Ren et al., 2001). However, nonlinear and nonequilibrium are the essence of the multiscale structure, as Li and Kwauk (1999) stated. So, it is very significant that a combination of the multiscale method and the nonlinear analysis method, such as

Correspondence concerning this article should be addressed to G.-B. Zhao at this current address: Coal/Gas Utilization Research Group, Dept. of Chemical and Petroleum Engineering, University of Wyoming, Laramie, WY 82071.

the fractal and time-delay embedding theory, is used to study the complexity of fluctuation dynamics in a fluidization system. However, there are no research reports about it.

Gas–solid fluidization is characterized by its heterogeneous two-phase structure with complicated dynamic changes. Quantification of such dynamic changes becomes a research focus in this field due to its importance in heat and mass transfer. Various nonlinear-analysis methods have been used for analyzing the dynamic changes prevailing in fluidization, such as time-delay embedding theory (Daw et al., 1990, 1995; van den Bleek and Schouten, 1993a,b; Schouten et al., 1996; Marzocchella et al., 1997; Bai et al., 1997b, 1999; Zijerveld et al., 1998; Ji et al., 2000; Zhao et al., 2001a), fractal theory (Fan et al., 1990, 1993; Franca et al., 1991; Cabrejos and Klinzing, 1995; Bai et al., 1996, 1997a; Kikuchi et al., 1996; Karamavruc and Clark, 1997); solitons theory (Komatsu and Hayakawa, 1993; Harris and Crighton, 1994; Göz, 1998); and information theory (Karamavruc et al., 1995). In fact, all phenomena occurring in gas–solid fluidization are attributed to the nonlinear interaction between the particles and the fluid, which are two independent media with their own individual movement tendencies. It is difficult to use a unified rule to describe these two different directions. As for time-delay embedding and fractal analysis, although they have been used in the study of fluidization including fluidization regimes and transition (Franca et al., 1991; Zijerveld et al., 1998; Bai et al., 1999; Johnsson et al., 2000; Zhao et al., 2000, 2001b), flow structure (Bai et al., 1996, 1997a; Marzocchella et al., 1997), fluidized-bed scale-up (van den Bleek and Schouten, 1993a; Schouten et al., 1996, 1999), and monitoring, evaluation, and control of fluidization quality (Daw and Halow, 1993; Schouten and van den Bleek, 1998), they are unable to extract different components with distinct features from global signals. Furthermore, the dissipative structure in fluidized systems has been found to show multiscale characteristics and the coupling of multiple subprocesses, for which average parameters and lumped models are inadequate to tackle the intrinsic mechanism (Li, 2000). Therefore, resolution with respect to scale is necessary.

Pressure fluctuations have been extensively studied, including the cause of pressure fluctuations (Fan et al., 1981, and references therein), the nature of pressure fluctuations (Zhao et al., 2001a, and references therein), signal composition of pressure fluctuations (He et al., 1997, and references therein), and origin, propagation, and attenuations of pressure waves (van der Schaaf et al., 1998, and references therein) and so on. A great advantage of the study of pressure signals is that they include the effects of many different (dynamical) phenomena taking place in fluidized beds, such as gas turbulence, bubble formation, passage and eruption of bubbles, self-excited oscillations of fluidized particles, and bubble coalescence and splitting (Bi et al., 1995; van der Schaaf et al., 1998). But now that pressure fluctuations include such a variety of information, how can we resolve this information into different components belonging to different mechanisms, such as particle interaction? Also, what is the criterion of resolution?

The complexity of a gas–solid fluidized bed relies so much on the fluctuation of pressure signals, it is very helpful to gain a good understanding of the complex hydrodynamic behavior of fluidized beds by extracting key feature information from pressure fluctuations. Because wavelet analysis has great potential in signal processing and feature extraction, it has been widely studied in the fluidization field (Bakshi et al., 1995; He et al., 1997; Lu and Li, 1999; Li, 2000; Ren et al., 2001, Guo et al., 2002; Li, 2002). Based only on this consideration, in this work we applied Daubechies wavelets to decompose pressure signals into 1–9-level detail signals and ninth-level approximation signals. Then, Hurst analysis was used to analyze the multifractal characteristics of different level signals. By synthesizing different level pressure signals of similar fractal characteristics, as discussed earlier, we obtained pressure fluctuation signals that represent microscale, mesoscale, and macroscale interaction in a fluidized bed, respectively. The intrinsic complexity of decomposed pressure signals of the three scales were further studied by time-delay embedding theory.

Theory

Discrete wavelet transform

The wavelet transform (WT) is a newly developed time-frequency analysis method that has been shown to be a powerful tool in all the the areas dealing with signal analysis and processing. Compared with the traditional Fourier method, there are some important differences between them. WT is being applied to transient signal processing, an area where Fourier transform fails to reveal the local turbulence. The Fourier transform is of a fixed resolution at all frequency components and has time-averaging effects that fail to detect small local disturbances. In contrast, wavelet analysis transforms a signal in the time domain into the time-frequency domain. The decomposed parts of the signal are resolved such that the higher the frequency, the finer the resolution. Unlike the Fourier transform, the basis function of WT is narrow (has smaller level) at higher frequencies and broad (has larger level) at low frequencies. WT is, therefore, often referred to as a sort of mathematical microscope, because different parts of the signal under analysis can be examined by automatically adjusting the focus.

Due to its inherent time-level locality characteristics, the discrete wavelet transform (DWT) has received considerable attention in the area of digital signal-processing. The term "wavelet" refers to sets of function $\psi_{j,k}(t)$ formed by dilatations and translations of a single function called the mother wavelet $\psi(t)$. The wavelet basis defined by

$$\psi_{j,k}(t) = 2^{j/2}\psi(2^j t - k) \tag{1}$$

is an orthonormal basis for $L^2(R)$ (square integrable). The mother wavelet, $\psi(t)$, has a companion, the scaling function $\phi(t)$; they both satisfy the following two-scaling relation (refinement equation)

$$\begin{cases} \phi(t) = \sqrt{2} \sum_{n=0}^{N} h_n \phi(2t - n) \\ \psi(t) = \sqrt{2} \sum_{n=1-N}^{1} g_n \phi(2t - n) \end{cases} \tag{2}$$

where h_n and g_n are discrete low-pass filter and high-pass filter, respectively, and N is an odd integer. Generally speaking, there are different filter coefficients for different mother wavelets.

According to the theory of multiresolution analysis (Mallat, 1989; Rioul and Duhamel, 1992), DWT consists of decomposing the discrete signal, $x(n)$, into an ordered set of orthogonal approximation and detail functions, $A^j(n)$ and $D^j(n)$ ($j = 1, 2, 3, \ldots, J$), respectively, as in the following equations

$$A^{j+1}(n) = \sum_m h_{m-2n} A^j(m) \tag{3}$$

$$D^{j+1}(n) = \sum_m g_{m-2n} D^j(m) \tag{4}$$

The approximation functions are the high-level (low-frequency) components of the signal, and they can be extracted using a low-pass filter, h_n. On the other hand, the detail functions are the low-level (high-frequency) components of the signal and can be extracted using a high-pass filter, g_n. The original data are considered to be the level function coefficients at the highest level, that is, $A^0(n)$. Thus, the original signal passes through two complementary filters and decomposes at the first level into two signals $A^1(n)$ and $D^1(n)$. Then $A^1(n)$ is further decomposed into $A^2(n)$ and $D^2(n)$. The decomposition process is repeated until the desired decomposition level, J, is reached. Unfortunately, if this decomposition is done without downsampling, that is, throwing away every second data point, one would wind up with n samples in each of the approximation and detail functions. The downsampling process introduces an overlap in the spectrum of the approximation and detail functions. This error can be recovered by carefully choosing filters for the decomposition and reconstruction phases that are closely related. A reverse process is used for perfect reconstruction of the decomposed signal from its approximation and detail functions by inserting zero values between their samples. This is referred to as upsampling. Signal reconstruction can be presented as

$$A^{j-1}(m) = \sum_k h_{m-2k} A^j(k) + \sum_k g_{m-2k} D^j(k) \tag{5}$$

Thus, the decomposition and reconstruction processes are as presented in Figure 1.

Consequently, the original signal can be expressed as the summation of the approximations and the details in a multistep manner as follows

$$x(n) = D^1(n) + A^1(n) = D^1(n) + D^2(n) + A^2(n) = \cdots = \sum_{j=1}^{J} D^j(n) + A^J(n) \tag{6}$$

Here $A^{j+1}(n)$ is smoother than $A^j(n)$, since the finer feature in $A^j(n)$ [that is, $D^j(n)$]' subtracted in order to get $A^{j+1}(n)$. At each level, j, the detail and approximation components, D^j and A^j, lie with a frequency band given by

$$D^j: \left[2^{-(j+1)}fs, 2^{-j}fs\right]$$

$$A^j: \left[0, 2^{-(j+1)}fs\right], \qquad j = 1, 2, \ldots, J$$

where fs is the sampling frequency. Thus, each information level decomposed by a wavelet represents information of a different frequency band of original signals. The detail component at a low level corresponds to information about the high frequency of the original signals, and the approximation component at a high level corresponds to information about the low frequency of the original signals.

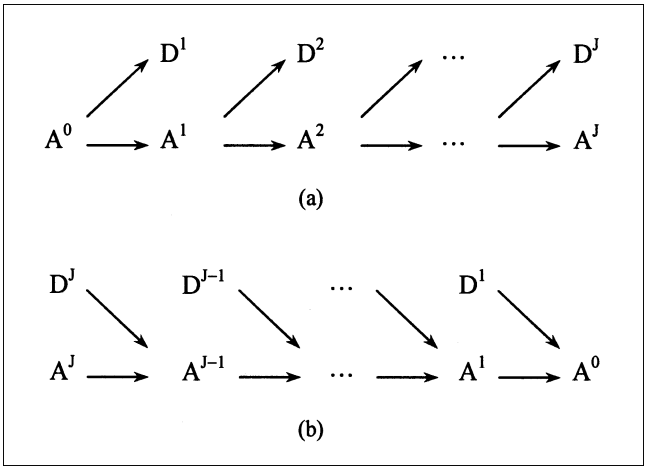

Figure 1. (a) Signal decomposition, and (b) reconstruction using the fast discrete wavelet algorithm at a different level.

Hurst analysis

Fan et al. (1990) were the first to apply the concept of fractional Brownian motion (fBm) for analyzing pressure fluctuations in a gas–liquid–solid fluidized bed in terms of Hurst's rescaled range (R/S) analysis. Hurst analysis was mainly used for flow-regime identification and classification (Franca et al., 1991; Drahos et al., 1992; Cabrejos and Klinzing, 1995; Maucci et al., 1999; Briens et al., 1997). In this work, we use this method as a criterion of the multiscale resolution of pressure fluctuations.

Rescaled range analysis, also referred to as range/standard deviation analysis, was originally developed about 50 years ago by Hurst (1951) to distinguish completely random time series from correlated time series. Mandelbrot and Van Ness (1968) formally related the Hurst exponent (H) to fractional Brownian motion, thus, making the H available as a descriptor to the scaling behavior of fractal curves, called self-similarity. The analysis begins with dividing a time series of length N into ml subseries of length τ (nonoverlapping). Next for each subseries $k = 1, 2, \ldots, ml$: (1) compute the mean, E_k, and standard deviation, S_k; (2) normalize the data $x_{i,k}$ by subtracting the sample mean $y_{i,k} = x_{i,k} - E_k$ for $i = 1, 2, \ldots, \tau$; (3) create a cumulative deviation $Z_{i,k} = \sum_{j=1}^{i} y_{j,k}$ for $i = 1, 2, \ldots, \tau$; (4) find the range $R_k = \max\{Z_{1,k}, Z_{2,k}, \ldots, Z_{\tau,k}\} - \min\{Z_{1,k}, Z_{2,k}, \ldots, Z_{\tau,k}\}$; (5) rescale the range R_k/S_k. Fi-

nally, the mean value of the rescaled range for the subseries of length τ is $(R/S) = (1/ml) \sum_{k=1}^{ml} (R/S)_k$.

After the analysis is conducted for all possible subseries lengths, τ, we can plot the (R/S) statistics against τ on a double-logarithmic coordinate. The Hurst coefficient, H, of the data set was then evaluated from the slope of the straight line fitted to these points in a least-square sense. H varies between 0 and 1. A Hurst exponent of 0.5 ($H = 0.5$) indicates that the series under examination behaves in a manner consistent with the random-walk theory. A Hurst exponent greater than 0.5 indicates persistence, and a value of less than 0.5 indicates antipersistence. For the persistent data set, if the trend or behavior in the data set is increasing or decreasing over a certain unit interval of time, it will continue to increase or decrease over such an interval. For this time-series data, H is related to its fractal dimension, D_F, by the relation $D_F = 2 - H$.

Time-delay embedding analysis

For a set of observable pressure fluctuating signals $x_1, x_2, \ldots, x_n$, it is difficult to distinguish whether the dynamics represented by this time series is random or deterministic. A low-dimensional attractor is usually employed to indicate the presence of deterministic behavior, so that a state vector in one dimension is reconstructed as follows

$$X_i = [x_i, x_{i+\tau}, \ldots, x_{i+(m-1)\tau}] \qquad i = 1, 2, \ldots, n-(m-1)\tau$$

in which, τ is a time delay and m is an embed dimension.

It is well known that the selection of an appropriate τ and m can ensure that the reconstructed vector is the topological equivalent of its primary data; moreover, m is well correlated with some chaotic invariants. Zhao et al. (2001a) discussed in detail the methods of determining time delay and embedding dimension. The same method and process were used to determine the reconstructed parameters, such as the embedding dimension and the time delay in this work. In order to approach the dynamics within a bubbling fluidized bed by using the pressure fluctuating data, two chaotic invariants, namely, correlative dimension (D_2) and Kolmogorov entropy (K-entropy), are used to characterize the motion process. The known formula representing the relationship between the correlation sum and the distance l is shown as follows

$$C_m(l) \propto l^{D_2} \tag{7}$$

In this equation, the exponent D_2 is the correlation dimension of the attractor, which represents the spatial correlation between measured points on the attractor. The definition of the correlation integral, $C_m(l)$, is

$$C_m(l) = \frac{1}{N_m(N_m-1)} \sum_{i \neq j} \theta\left(l - |\boldsymbol{X}_i - \boldsymbol{X}_j|\right) \tag{8}$$

where N_m is the total number of points evaluated, and $\theta(x)$ is the Heaviside function, as follows

$$\theta(x) = \begin{cases} 1 & x \geq 0 \\ 0 & x < 0 \end{cases} \tag{9}$$

The definition of K-entropy is let a trajectory (on an attractor) evolve for a long time, and then calculate the entropy's average rate of increase with respect to sequence length. Grassberger and Procaccia (1983a,b) also proposed the relationship between K-entropy with D_2, and its formulated expression is

$$C_m(l) = l^{D_2} 2^{-K_2 m\tau} \tag{10}$$

From Eq. 10, we have

$$\log_2 C_m(l) = D_2 \log_2 l - K_2 m\tau \tag{11}$$

by plotting $\log_2 C_m(l)$ vs. $\log_2 l$ for values of m equal to 2 or more. Each curve exhibits a region of linearity called the no-scale interval, the slope of which corresponds to D_2. As the dimension, m, is increased beyond the embedding dimension, the slope of the linear region of the curves yields a consistent value of D_2, and these curves are displaced from each other by a factor of $-m\tau K_2$. In the literature (Cohen and Procaccia, 1985; Cassanello et al., 1995), the methods for evaluating the correlation dimension and the K-entropy from Eq. 11 have been discussed. However, the proposed methods are very complicated, and the two chaotic parameters are estimated separately. In view of these facts, Zhao et al. (1999, 2001b) proposed an optimal algorithm for computing simultaneously the correlation dimension and K_2 entropy by a least-square method. Generally speaking, K_2 entropy can be considered as a measure of the rate of information loss along the attractor or a measure of the degree of predictability of points along the attractor, given an arbitrary initial point. Therefore, the larger the value of K_2 entropy, the more complex the system studied. A zero entropy represents a constant or a regular cyclic phenomenon that can be represented in the state space by a fixed point, a periodic attractor, or a multiperiodic attractor. An infinite entropy refers to a stochastic, nondeterministic phenomenon.

Experimental Studies

The experiments were carried out in a 0.3-m-diam. and 3-m-high column described previously (Zhao et al., 2001a). The fluidized-bed assembly includes a bed column, a distributor, and a plenum chamber. The polyethylene (PE) particle used as the fluidized particle has a density of 960 kg/m^3, and average diameter of 500 μm. Its minimum fluidized-gas velocity u_{mf} is 0.118 m/s, and it has a static-bed eight of 0.46 m. The fluidizing fluid is air. The experimental range of the gas flow rate is $u/u_{mf} = 1.0 \sim 5.6$. The holes on the distributor were 2 mm in diameter and gave a fractional open area of 4%. Four piezoresistive pressure transducers (CYG219 type, Baoji Research Center of Transducer, China) were used to measure local pressure fluctuations. Pressure probes were installed on the wall of the bed column at four different heights from the distributor: 0.090 m, 0.20, 0.40 m above it, and 0.12 m below it, corresponding data run numbers C1, C2, C3, C4, respectively. Each pressure probe was connected to one of the two input channels of the differential pressure transducer, which produced an output voltage proportional to the pressure difference between the two channels. The remaining channel

was exposed to the atmosphere. The differential range of the pressure transducer was ± 4 kPa, and the relative accuracy was $\pm 0.1\%$ full scale. The time series consisted of at least 60,000 points and were sampled at a frequency of 250 Hz using an analog-to-digital converter with a 12-bit nominal resolution.

Results and Discussion

Daubechies wavelet decomposition of pressure fluctuations

There are many types of wavelets, such as Harr, Daubechies, Mexican hat, and Spline wavelet. One can choose among them depending on a particular application. As Tewfik et al. (1992) showed, the quality of signal decomposition and reconstruction is highly dependent on the selection of the mother wavelet. Wavelets being of compact support and orthogonality are very significant for both theoretical research, and practical application, especially since they can provide a limited and more practical digital filter in the process of wavelet decomposition of digital signals. However, Daubechies' wavelets of different compact support possess only these properties and have some smoothness (Daubechies, 1988). Therefore, in this work we use Daubechies wavelets for decomposing pressure signals.

In Daubechies wavelets, the time domain of wavelet function is limited, that is, compactly supported in time. And, the wavelet function $\psi(t)$ has L-order consecutive moments equal to zero. That is

$$\int t^p \psi(t)\, dt = 0, \qquad p = 0, 1, 2, \ldots, L \tag{12}$$

The time domain of the wavelet function increase with L. Because of the size of L, we called the Daubechies wavelet DAUL wavelet in this work. For example, we called them DAU5 wavelets when L was equal to 5.

The Daubechies wavelet function $\psi(t)$ is the weight sum of the level function $\phi(2t)$ by shifting

$$\psi(t) = \sqrt{2} \sum_{n=1-N}^{1} g_n \phi(2t - n) \tag{13}$$

Therefore, compact support of function $\psi(t)$ in the time domain is $t \in [1 - L,\ L]$. The level function is a function of the low-pass filter, and the filter coefficients are h_n ($n = 1, 2, \ldots, N$). The filter coefficients of the high-pass filter corresponding to the wavelet function are g_n, and have

$$g_n = (-1)^n \cdot h_{1-n} \tag{14}$$

In the literature (Daubechies, 1988), Daubechies provided nine sets of filter coefficients corresponding to L from 2 to 10.

As discussed earlier, Daubechies wavelets are good enough to have an engineering application, and the choice of analyzing wavelets plays a significant role in signal processing. However, Daubechies wavelets with different compact support can give rise to different decomposition errors, as Qi (2000) pointed out. It is, therefore, very important to choose the compact support Daubechies wavelet with minimum decomposition error as the optimal wavelet for the resolution of pressure signals. According to Eq. 6, original signals $x(n)$ are changed to $\hat{x}(n)$ by the algorithm of decomposition and reconstruction shown in Figure 1, as follows

$$\hat{x}(n) = A^J(n) + \sum_{j=1}^{J} D^j(n) \tag{15}$$

We defined decomposition error between original signals $x(n)$ and reconstructed signals $\hat{x}(n)$ as E_L for a different compact support Daubechies wavelet, DAU L. That is

$$E_L = \frac{1}{NT} \sum_{k=1}^{NT} |x(k) - \hat{x}(k)| \tag{16}$$

It is, thus, clear that the different decomposition error can be found for a different DAU L (that is, Daubechies L wavelet) corresponding to a different filter coefficient, h_n and g_n.

It is worth noting that we have analyzed experimental data at different gas velocities from different data runs and have obtained nearly the same results as in the following. To simplify things for the following discussion, we only illustrate the results at $u = 0.299\ \mathrm{m \cdot s^{-1}}$ as an example. We believe that the results we have obtained are of universal significance in the bubbling flow region. Decomposition errors of pressure signals at $u = 0.299\ \mathrm{m \cdot s^{-1}}$ for data-run number C1 are shown in Table 1 using different Daubechies wavelets at levels from 1 to 9 in the light of Eqs. 15 and 16. It is clear that decomposition errors are minimum using DAU2 at different levels. Decomposition errors reach maximum using DAU10 at dif-

Table 1. Decomposition Errors of Pressure Fluctuations Using Different Daubechies Wavelets at $u = 0.299\ \mathrm{m \cdot s^{-1}}$ for Data-Run Number C1

	Level								
DAU	1	2	3	4	5	6	7	8	9
2	0.000005	0.000008	0.000010	0.000012	0.000015	0.000016	0.000017	0.000017	0.000017
3	0.000011	0.000028	0.000050	0.000090	0.000201	0.000213	0.000477	0.000694	0.005593
4	0.000025	0.000061	0.000113	0.000116	0.000775	0.000742	0.001266	0.001740	0.014536
5	0.9699	1.5436	1.4372	1.1060	1.3676	1.4827	1.5249	1.5280	1.5344
6	0.16312	0.26173	0.24522	0.17612	0.21518	0.21961	0.22888	0.22919	0.26148
7	0.000129	0.000131	0.000279	0.000577	0.006368	0.007632	0.008106	0.008566	0.054575
8	0.000113	0.000153	0.000678	0.001843	0.009967	0.009949	0.014081	0.15672	0.052329
9	0.000102	0.000131	0.000857	0.001778	0.006319	0.013380	0.018948	0.022461	0.040224
10	12.7749	24.2605	30.9408	28.9140	21.1536	18.1852	18.3398	18.3309	18.3250

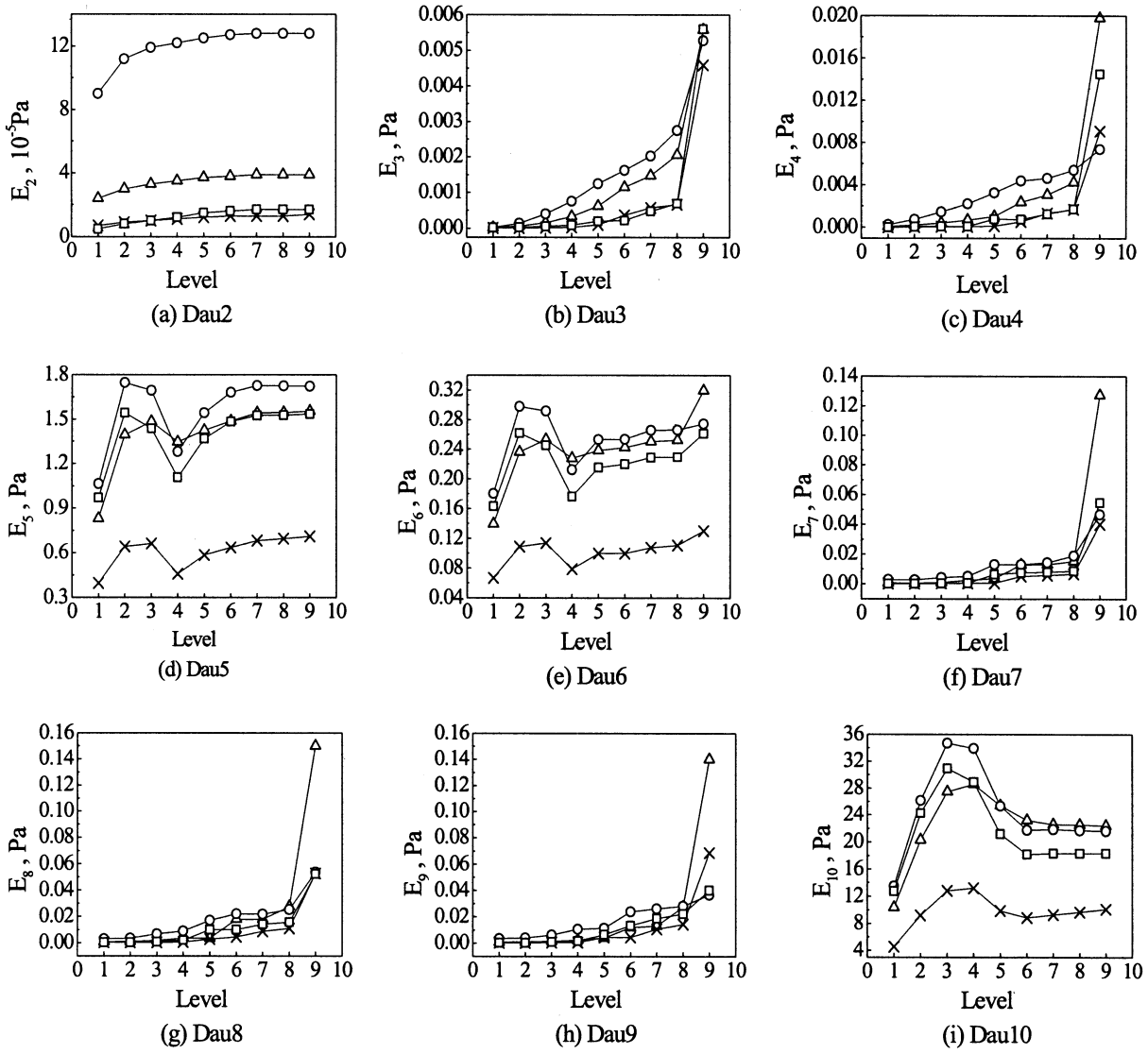

Figure 2. Decomposition errors of pressure fluctuations for different Dau L ($L = 2 \sim 10$) at $u = 0.299\ \mathrm{m \cdot s^{-1}}$.

Data-run number: C1 (□); C2(○); C3(△); C4(×).

ferent levels, and relatively large errors are reached by DAU5. For the same Daubechies wavelet, decomposition error generally increases with the decomposition level, such as DAU(2–4) and DAU(7–9). However, there are maximum decomposition errors at level 2–4 for DAU10, DAU5, and DAU6. Decomposition errors of pressure fluctuations at different measurement locations using different Daubechies wavelets are shown in Figure 2 for different decomposition levels ($J = 1, 2, \ldots, 9$). This shows a similar trend for decomposition errors with the decomposition level for pressure signals measured at different locations, but there is a large difference among decomposition errors for pressure signals measured at different locations at the same decomposition level. Therefore, we should pay attention to the influence of different Daubechies wavelets on decomposition results when wavelet decomposition and feature information extraction of pressure signals are conducted in fluidized beds. Nevertheless, we find that the order of magnitude of decomposition errors using DAU2 is as low as 10^{-4}; it is the smallest of the decomposition errors of different Daubechies wavelets. So, DAU2 can be seen as the optimal Daubechies wavelet of decomposition of pressure fluctuations. The level function and wavelet function of DAU2 are shown in Figure 3. The filter coefficients of DAU2 are as follows

$$h_n = [0.4829629131445341,\ 0.8365163037378077,\ 0.2241438680420134,\ -0.1294095225512603]$$

$$g_n = [-0.4829629131445341,\ 0.8365163037378077,\ -0.2241438680420134,\ -0.1294095225512603]$$

Figure 4 illustrates decomposition of pressure signals using DAU2 as the 1–9-level detail signals and ninth approximation signal (corresponding to $J = 9$) at $u = 0.299\ \mathrm{m \cdot s^{-1}}$ for data run number C1. Therefore, the DAU2 wavelet is chosen as the wavelet of pressure-signal decomposition in the following study.

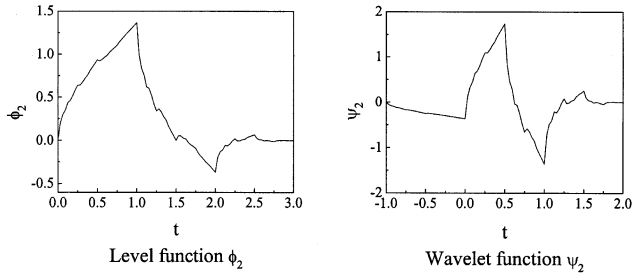

Figure 3. Daubechies second-order level function and wavelet function.

Multifractal characteristics of decomposed signals of pressure fluctuations

Figure 5 shows that the rescaled range (R/S) for decomposed 1−9-level detail signals and ninth approximation signal (corresponding to $J = 9$) at $u = 0.299$ m·s^{-1} for a different data-run number using DAU2, varied with subseries length τ in log-log coordinates, as illustrated earlier. To increase the accuracy of the slope H at long subseries lengths, the record length is first increased to 50,000 points for the total sampling time of 200 s. R/S as a function of τ is evaluated for 25 different starting conditions, and the average values are plotted in these figures. It is clear that $\log(R/S) \sim \log \tau$ shows similar behavior for decomposed pressure signals from four different measurement locations. That is, only one Hurst exponent, H, corresponding to only linear relationship of $\log(R/S) \sim \log \tau$ can be obtained for decomposed level 1 and 2 detail signals and level-9 approximation signal. However, two distinct Hurst exponents can be derived for decomposed 3−9-level detail signals, corresponding to two distinct linear relationship of $\log(R/S) \sim \log \tau$ at smaller τ and larger τ. This suggests a bifractal structure of decomposed 3−9-level detail signals. Hurst exponents, H, of decomposed signals for different measurement locations are shown in Table 2 as a linear regression of the straight portion of the curves shown in Figure 5. Although there is a smooth transition between two regions for signals $D^3 - D^9$, the transition points as shown

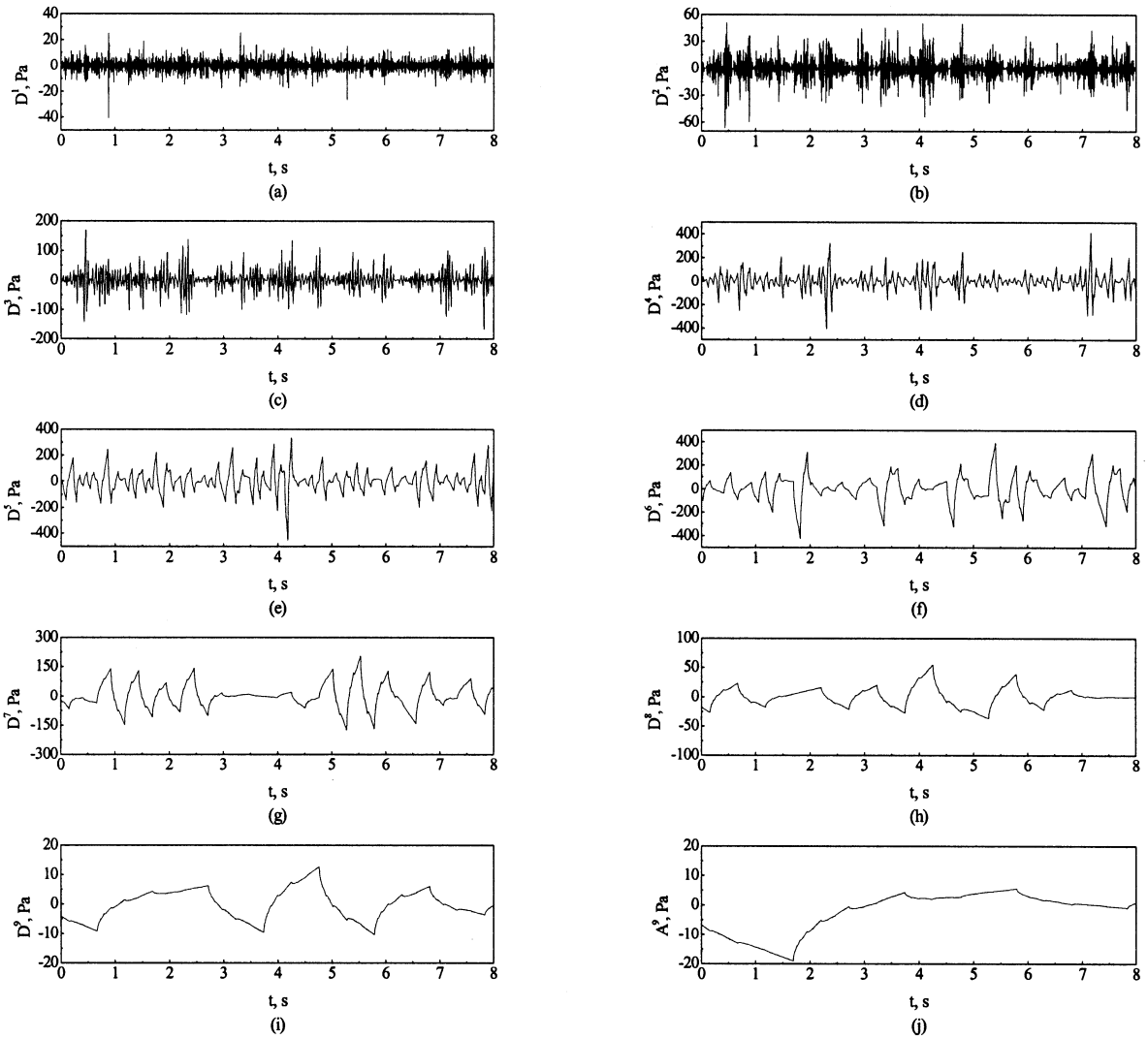

Figure 4. Decomposed signals of pressure fluctuations using DAU2 at $u = 0.299$ m/s for data-run number C1.

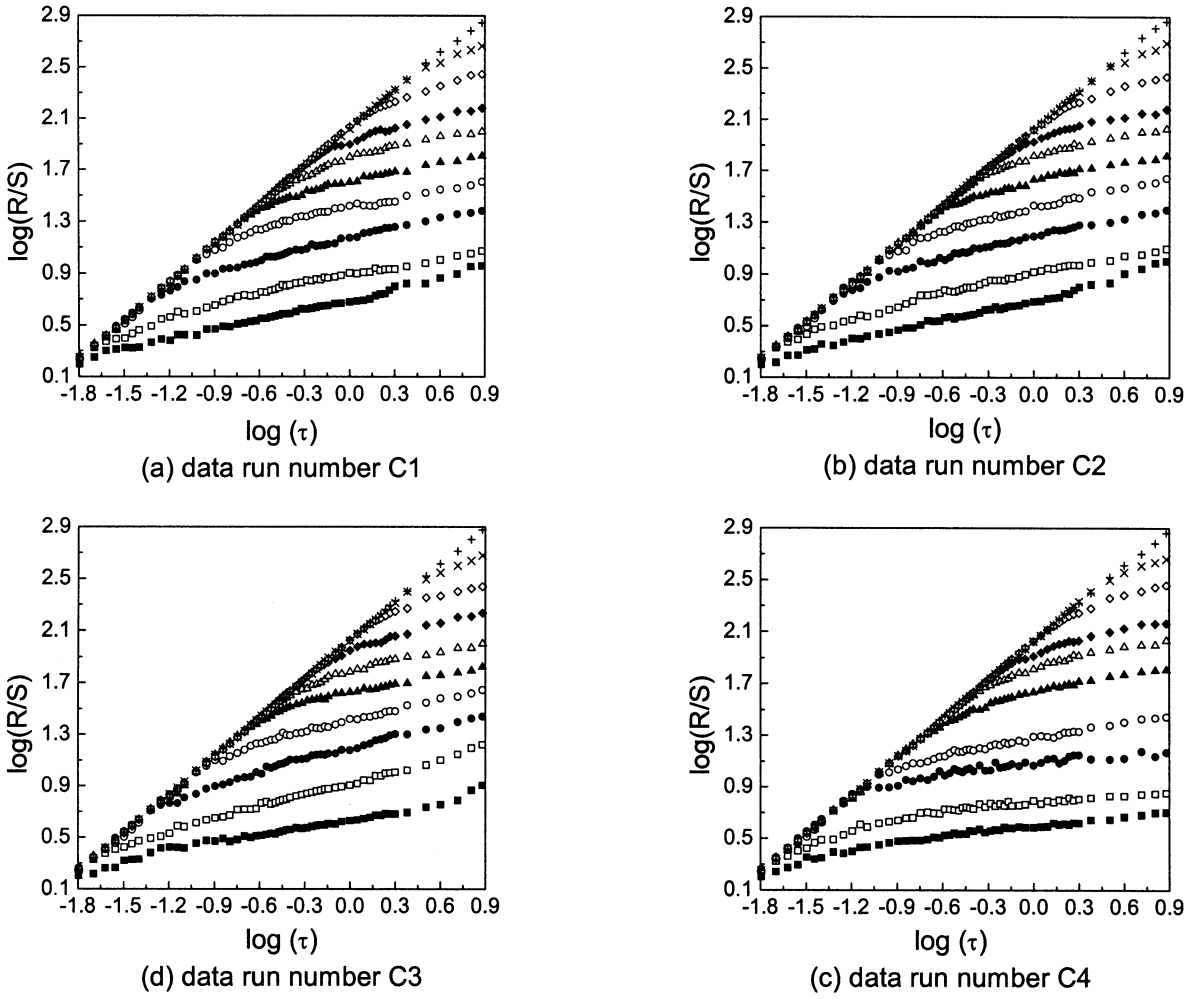

Figure 5. $\log(R(\tau)/S(\tau)) \sim \log \tau$ for decomposed signals for different data run number.

Decomposed signal: D^1 (■); D^2 (□); D^3 (●); D^4 (○); D^5 (▲); D^6 (△); D^7 (◆); D^8 (◇); D^9 (×); A^9 (+).

in Figure 5 are fairly small. However, these transition points wouldn't affect the computation accuracy. Briens et al. (1997) found that Hurst exponents achieve a smooth transition between the two regions by applying a smooth spline to the original $\log(R/S) \sim \log\tau$ curves.

The reciprocal of the break point τ, between the two linear regions is similar to the domain frequency of the signal. Fan et al. (1993) pointed out that a break in the rescaled range at time lag τ can be caused by one major periodic component of the signal. Our results appear to be consistent with this finding, as demonstrated in Figure 5, where there is a dominant frequency of 18–20 Hz corresponding to $\log \tau = (-1.26)$–(-1.32) for the signal D^3, 7.9–11 Hz corresponding to $\log \tau = (-0.90)$–(-1.05) for the signal D^4, 3.98–5.0 Hz corresponding to $\log \tau = (-0.6)$–(-0.7) for the signal D^5, 2.0–3.16 Hz corresponding to $\log \tau = (-0.50)$–(-0.30) for

Table 2. Hurst Exponents of Decomposed Signals for Different Measurement Locations at $u = 0.299$ m · s^{-1}

Location (m)		Signal									
		D^1	D^2	D^3	D^4	D^5	D^6	D^7	D^8	D^9	A^9
0.090	H_1	[—]	[—]	0.978	0.986	0.986	0.983	0.987	0.986	0.995	0.987
	H_2	0.252	0.283	0.279	0.258	0.262	0.254	0.288	0.406	0.459	[—]
0.20	H_1	[—]	[—]	0.944	0.988	0.983	0.984	0.992	0.989	0.992	0.992
	H_2	0.263	0.271	0.272	0.278	0.284	0.291	0.239	0.362	0.469	[—]
0.40	H_1	[—]	[—]	0.959	0.968	0.986	0.986	0.998	0.994	0.990	0.991
	H_2	0.213	0.289	0.314	0.284	0.232	0.239	0.324	0.354	0.482	[—]
−0.12	H_1	[—]	[—]	0.940	0.970	0.983	0.983	0.991	0.995	0.995	0.988
	H_2	0.224	0.219	0.241	0.233	0.229	0.257	0.288	0.384	0.423	[—]

the signal D^6, 1–1.38 Hz corresponding to log $\tau = (-0.14)$–0 for the signal D^7, 0.66–0.69 Hz corresponding to log $\tau =$ 0.16–0.18 for the signal D^8, and 0.31–0.42 Hz corresponding to log $\tau = 0.38$–0.51 for the signal D^9. This is also consistent with the frequency band of wavelet transformation given by, D^j: $[2^{-(j+1)}f_s, 2^{-j}fs]$.

The following features are observed from Table 2 and Figure 5. These results, obtained from Hurst analysis, will be further demonstrated by the time-delay embedding analysis presented below. (1) Level 1 and 2 detail signals show monofractal characteristics for pressure signals measured at different locations. The Hurst exponents of these signals are found to be much lower than 0.5, so they represent an antipersistent dynamic behavior in the fluidized bed. Because the low Hurst exponents correspond to signals with little persistence (highly chaotic) (Karamavruc and Clark, 1997a), level 1 and 2 detail signals imply microscale interaction between discrete individual particles and fluid and among individual particles, since the motion of solids is highly random. And, according to wavelet analysis, level 1 and 2 detail signals represent information about the high frequency of the original pressure signals, as is the high-frequency behavior of the interaction among particles and between particles and fluid. Thus, it is plausible that level 1 and 2 detail signals are seen as a microscale interaction in a fluidized bed. (2) Level 3–9 detail signals show a bifractal characteristic of fluidization dynamics. Bifractal flow behavior has also been observed for gas–liquid two-phase flows (Franca et al., 1991; Kozma et al., 1996) and gas–solids fluidized beds (Bai et al., 1997b, 1999), and appears to be characteristic of a number of heterogeneous multiphase flows. Two distinct Hurst exponents, H_1 being the slope at smaller τ and H_2 the slope at larger τ, are shown in Figure 5 for these signals. Hurst exponent H_1 at smaller τ is much larger than 0.5, as shown in Table 2, which indicates a highly persistent dynamic feature of the fluidized system. On the other hand, Hurst exponent H_2 at larger τ is much less than 0.5, which indicates a highly antipersistent dynamic feature of the fluidized system. As Karamavruc and Clark (1997a) stated, bubble motions correspond, in general, to higher Hurst components than do particle motions. All of these indicate to a great extent that level 3–9 detail signals reflect mesoscale interaction between the bubble phase and the dense phase, while H_1 at smaller τ represents a dynamic feature of the bubble phase and H_2 at larger τ represents dynamic feature of the dense phase. (3) Level 9 approximation signals are of a persistent dynamic feature, with a sole Hurst exponent much larger than 0.5. Since level 9 approximation signals represent the fluctuation dynamics of the whole fluidized bed from a much higher level, its Hurst exponent H_1, which is close to unity, shows that these signals reflect the macroscopic stability of the whole bed. Therefore, level 9 approximation signals represent the macroscale interaction of the bed. Fractal dimensions corresponding to different-level signals on the basis of Hurst exponents are shown in Figure 6 (for ease of explanation, level 10 in Figure 6 is actually a level 9 approximation). As Mandelbrot and Van Ness (1968) stated, fractal dimension $D_F = 2 - H$ represents the self-similarity of the curves studied. The larger the value of D_F, the more rough and antipersistent the curves of pressure fluctuations, and the more complex the corresponding dynamic. Therefore, in Figure 6 it can also be seen that microscale interaction corresponding to particle motion is more complex than mesoscale interaction, which agrees with the bubbling motion. This is a reason why many studies applied a stochastic model to study particle motion and applied a deterministic model to study bubbling motion.

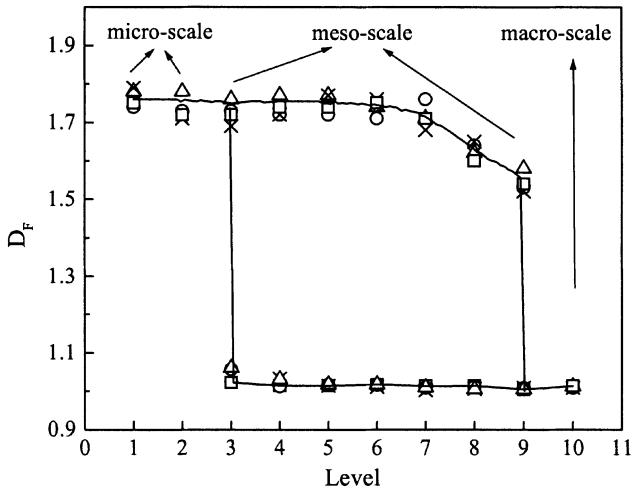

Figure 6. Fractal dimension vs. level for different data-run number at $u = 0.299$ m·s^{-1}.

Data run number: C1 (□); C2 (○); C3 (×); C4 (△).

Multiscale characteristics of pressure fluctuations

As analyzed earlier, multifractal characteristics of pressure signals can be well understood by R/S analysis after decomposition using the wavelet method. However, the dynamics of the bubbling phase belonging to the mesoscale interaction is almost identical to the dynamics of the macroscale interaction, because of their similar fractal dimension and Hurst exponent (Figure 6 and Table 2). That is not the case, because there is a large difference in dynamics between mesoscale and macroscale interaction by analysis of the fluidizing mechanism, as discussed by Li et al. (1999). This indicates that R/S analysis is not a good method for distinguishing dynamic behavior between mesoscale and macroscale interaction. We need another theory to quantify them. This causes us to study these differences further, using the time-delay embedding theory (see below). In addition, fractal dimension and Hurst exponents are also almost identical between 1 and 2 level microscale signals and 3–7 level, mesoscale signals representing the dynamics of the dense phase. But Hurst exponents begin to increase for 8 and 9 level detail signals, which corresponds to when the fractal dimension begins to decrease. This indicates that the dynamics of microscale interaction between individual particles and fluid are different from those of the dense phase of mesoscale interaction. Furthermore, interaction between individual particles and fluid is more random and complex. Differences of fractal dimension and Hurst exponents representing the dense phase at different wavelet decomposition levels at the same mesoscale demonstrate that the coupling of multiple subprocesses existed in mesoscale interaction, as suggested by Li (2000).

Pressure fluctuations in a fluidized bed are a complex function of particle properties, bed geometry, properties, and

the flow condition of the fluidizing fluid (Fan et al., 1981). We found that pressure fluctuations caused by different factors can be resolved from measured signals by means of Hurst analysis. For example, microscale interaction pressure signals representing the dynamics of individual particles can be obtained by synthesizing level 1 and 2 detail signals because of their similar fractal feature. Pressure signals of mesoscale interaction representing the dynamics of the dense phase and the bubbling phase can be obtained by synthesizing level 3–9 detail signals because of their similar bifractal feature. Level 9 approximation signals representing the global system of particle–fluid suspension within its boundaries, are macroscale signals. An example of three-scale resolution is shown in Figure 7 for data-run number C1 at $u = 0.299$ m·s^{-1}. These results are consistent with those of Li and Kwauk (1994), which indicated that particle and the fluid interaction may be considered on three scales: microscale (individual particles and fluid), mesoscale (cluster and dilute phase; or bubble and emulsion), and macroscale (effect of the equipment).

The energy of a digitized signal can be defined as the squared sum of amplitude as follows

$$W = \sum_{i=1}^{N} |x(i)|^2 \tag{17}$$

Let W_j be defined as level j energy, which is the decomposed cumulative energy of different level j detail signals on the basis of Eq. 6. Namely

$$W_j = \sum_{i=1}^{N} |D^j(i)|^2 \qquad (i = 1, 2, \ldots, J) \tag{18}$$

with the total energy given by

$$W_T = \sum_j W_j \tag{19}$$

To be more precise, the ratio of energy at different levels to the total energy is more important in showing how the energy is displayed at different levels. Let

$$R_j = \frac{W_j}{W_T} \times 100\% \tag{20}$$

where W_T is determined by Eq. 19. In this manner, R_j gives a relative energy distribution in each level.

The energy profile for the decomposed signals using DAU2 at $u = 0.299$ m·s^{-1} is shown in Figure 8 for a different data-run number. As before, for simplicity, the explanation of level

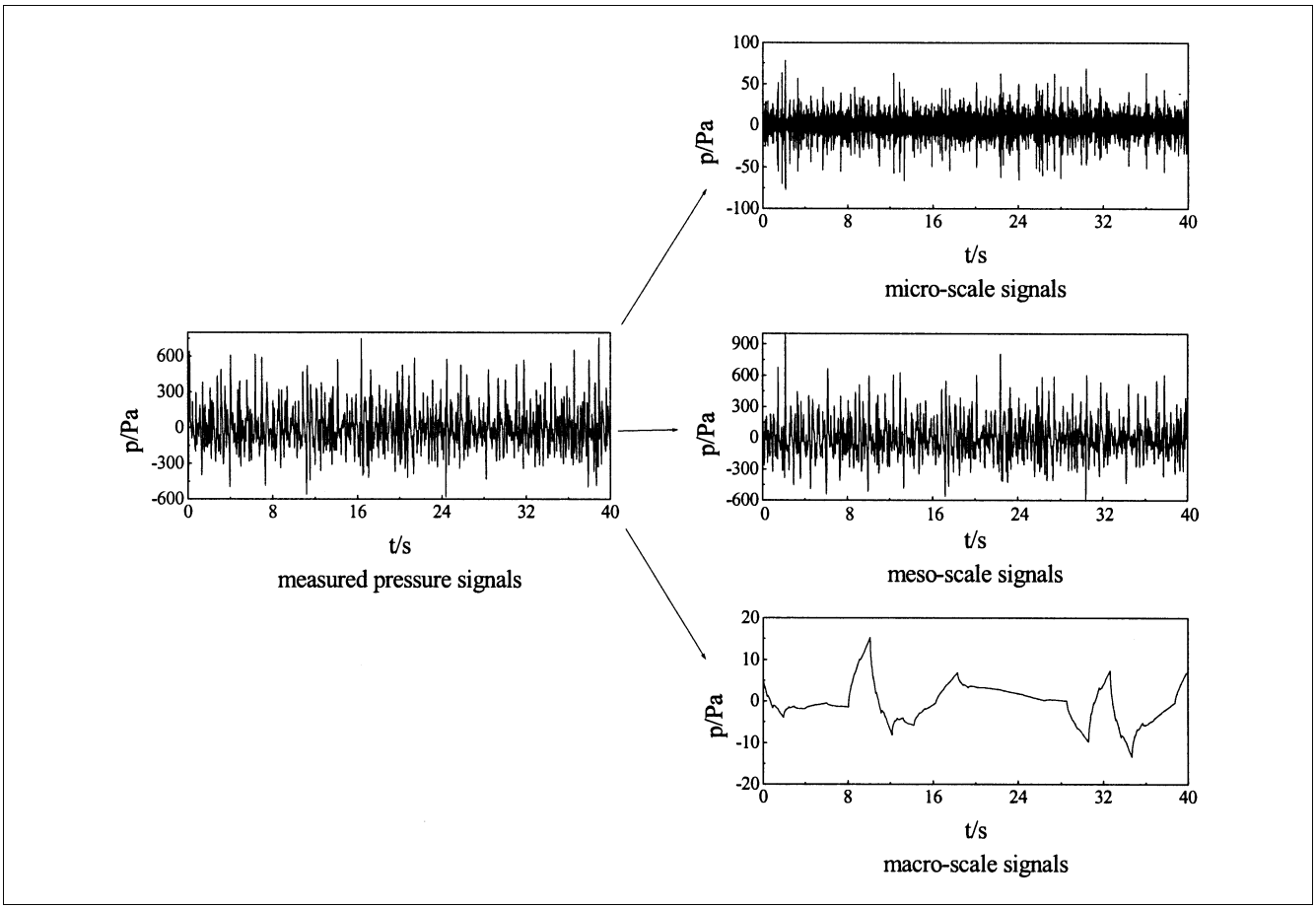

Figure 7. Resolution of measured pressure fluctuations into three scales for data-run number C1.

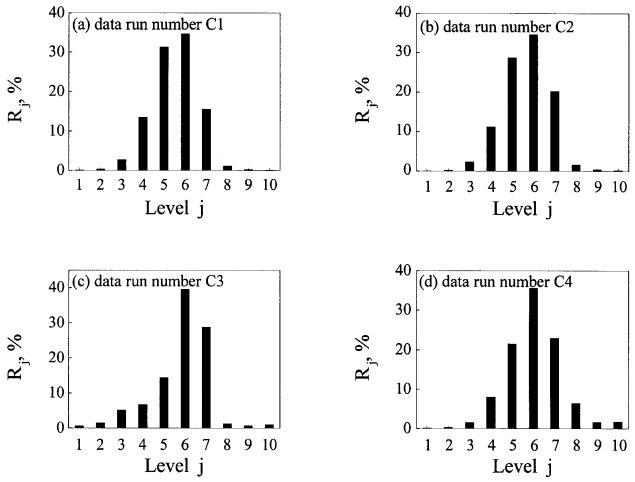

Figure 8. Energy profiles for different level signals at $u = 0.299\ \mathrm{m \cdot s^{-1}}$.

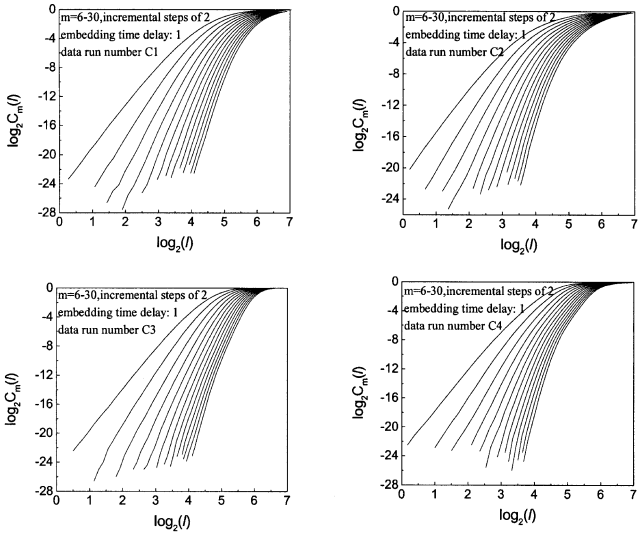

Figure 9. $\log_2 C_m(l) \sim \log_2(l)$ of microscale signals for different data-run numbers.

10 in Figure 8 is actually a level 9 approximation. It can be seen that the most energy is distributed mainly by mesoscale signals of the level 3–9 detail, and is over 90% of the total energy. The energy of microscale and macroscale signals is very low. The distribution of the total energy among the three scales of micro, meso, and macro is shown in Table 3. All of these also indicate that pressure fluctuations mainly reflect mesointeraction between the emulsion phase and the bubbling phase. The low frequency and amplitude of macroscale signals demonstrate macrostability of the fluidizing system observed from a macroscopic whole. Therefore, the fluidizing system is a wholely stable and locally unstable system with a multiscale structure at normal fluidizing conditions.

Time-delay embedding analysis of three-scale resolution signals

The relationship of $\log_2 C_m(l)$ vs. $\log_2 l$ of various scale pressure signals from different data-run numbers, are shown in Figures 9, 10, and 11, respectively. We found that two no-scale intervals existed for mesoscale signals. Therefore, there are two correlation dimensions, $D_{2,1}$ and $D_{2,2}$, and two K_2-entropies, $K_{2,1}$ and $K_{2,2}$, representing the dynamics of the emulsion phase and the bubbling phase, respectively. The linear part of the correlation dimension at a smaller region is associated with the dense phase, whereas the linear part at a larger region is associated with the bubble phase. That is to say, the invariant slope in a smaller region is the correlation dimension of the subregion, which is characteristic of a particle cluster, and the invariant slope in a larger region is the correlation dimension of the region, which is characteristic of a bubble motion. Similar results have been demonstrated by Bai et al. (1997b, 1999), Karamavruc and Clark (1997b), and Zhao et al. (2001b). The computed correlation dimension and K_2-entropy of various-scale pressure signals from different data-run numbers are shown in Table 4. Comparison between fractal dimension in Figure 6 and the correlation dimension in Table 4 shows that their differences are very large. As Tsonis (1992) illustrated, we must note that the concept of fractal dimension can be applied to time series in two distinct ways. The first is to indicate the number of degrees of freedom in the underlying dynamical system. The second is to quantify the self-similarity of the trajectory in phase space. The Grassberger–Procaccia algorithm yields the first one, but does not really provide an estimate of the self-similarity of the trajectory. As discussed earlier, however, the fractal dimension yielded by R/S analysis depicts the self-similarity of the studied signals.

It also can be seen from Table 4 that the correlation dimension $D_{2,1}$ and K_2-entropy, $K_{2,1}$, of the microscale signals representing individual particle motion are larger than the correlation dimension $D_{2,2}$ and K_2-entropy, $K_{2,2}$, of the mesoscale signals representing the dense-phase motion, and the correlation dimension $D_{2,1}$ and K_2-entropy, $K_{2,1}$, of the mesoscale signals representing the bubbling-phase motion are larger than those of macroscale signals representing the dynamics of the entire fluidizing system. These results indicate that the dynamics of individual particles is more complex than that of particle clusters, that is, the dense phase and the dynamics of the bubbling phase are more complex than those of the whole fluidized bed. However, these conclusions cannot be obtained from the fractal dimension of R/S analysis, as discussed earlier. There are, therefore, many advantages to combining several interdisciplinary analysis methods to study

Table 3. Energy Distribution for Multiscale Signals

Data	Data-Run Number C1			Data-Run Number C2			Data-Run Number C3			Data-Run Number C4		
Scale	Micro	Meso	Macro	Micro	Meso	Macro	Micro	Meso	Macro	Micro	Meso	Macro
R_s	0.44%	99.42%	0.14%	0.33%	99.39%	0.28%	2.20%	96.84%	0.96%	0.45%	97.86%	1.69%

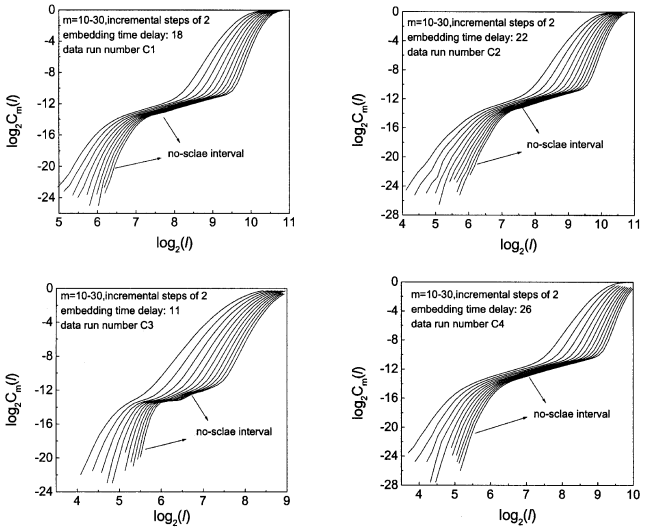

Figure 10. $\log_2 C_m(l) \sim \log_2(l)$ of mesoscale signals for different data-run numbers.

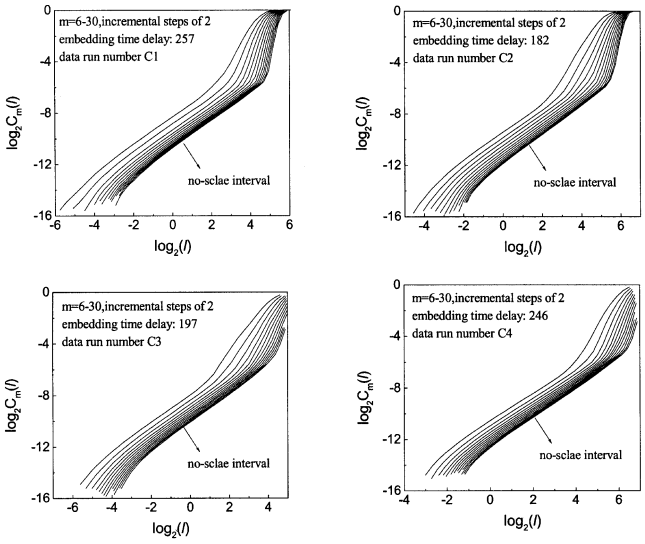

Figure 11. $\log_2 C_m(l) \sim \log_2(l)$ of macroscale signals for different data-run numbers.

the complex dynamics of the fluidizing system, especially combining manifold nonlinear approaches. In addition, the correlation dimension $D_{2,2}$ and K_2-entropy, $K_{2,2}$, of the dense phase is much larger than the correlation dimension $D_{2,1}$ and K_2-entropy, $K_{2,1}$, of the bubbling phase at the same mesoscale. It is further confirmed that the dynamics of the bubble motion is more uncomplicated and easy to describe, and the dynamics of the particle motion is more complex and hard to exactly describe.

Conclusions

This work combines multiple analytical approaches, including wavelet transform, rescaled-ranged analysis, multiscale resolution, and time-delay embedding, to study pressure fluctuations in a bubbling fluidized bed. The main findings of the present work can be summarized as follows:

1. Daubechies wavelets are used to decompose the time series of pressure fluctuations to level 1–9 detail signals and level 9 approximation signals. We found that the Daubechies second-order (DAU2) wavelet is optimal, because of its minimum decomposition residuals for pressure signals at different measurement locations. We, therefore, chose the DAU2 wavelet as the wavelet of decomposition of the pressure signals in this study.

2. Hurst analysis is used to analyze multifractal characteristics of the decomposed different-level signals. The research shows that level 1 and 2 detail signals have only one Hurst exponent much less than 0.5; level 3–9 detail signals have two Hurst exponents, one larger than 0.5 at smaller τ and one less than 0.5 at larger τ, respectively; and the level 9 approximation signal has only one Hurst exponent much larger than 0.5. These results indicate that level 1 and 2 detail signals reflect microscale dynamics, level 3–9 detail signals represent mesoscale dynamics, and level 9 approximation signals represent macroscale dynamics. It is conjectured that the microscale dynamics result from individual particles motion and small-scale fluid eddies, the mesoscale dynamics result from bubble dense phase interactions, and the macroscale dynamics result from large bulk motions of the solids at the scale of the whole bed.

3. Therefore, measured pressure signals can be reduced to multiscale signals such as microscale signals, mesoscale signals, and macroscale signals. Microscale and macroscale signals have monofractal characteristics, while mesoscale signals have bifractal characteristics. By analyzing the energy profiles of the different scale signals, we found that the most energy is distributed mainly by mesoscale signals of the level 3–9 detail and is over 90% of the energy. Pressure fluctuations, therefore, mainly reflect mesointeraction between the emulsion phase and the bubbling phase.

4. Time-delay embedding analysis of different-scale signals revealed that the microscale dynamics is more complex than that at mesoscale, and the mesoscale dynamics is more complex than that at macroscale. However, these conclusions cannot be obtained from the fractal dimension of R/S analysis. Therefore, we emphasized that multiple analytical approaches can be more appropriate for characterizing the complexity of a fluidized system.

Table 4. Correlation Dimension and Kolmogorov Entropy for Multiscale Signals

Data	Data-Run Number C1			Data-Run Number C2			Data-Run Number C3			Data-Run Number C4		
Scale	Micro	Meso	Macro	Micro	Meso	Macro	Micro	Meso	Macro	Micro	Meso	Macro
$D_{2,1}$	13.28	1.47	1.14	14.06	1.44	1.23	14.13	1.51	1.19	15.09	1.39	1.22
$K_{2,1}$	119.22	0.558	0.0728	140.55	0.465	0.0783	94.68	1.36	0.0777	127.25	0.842	0.0722
$D_{2,2}$		10.80			8.74			9.96			8.64	
$K_{2,2}$		3.84			5.64			10.42			3.92	

Literature Cited

Bakshi, B. R., H. Zhong, P. Jiang, and L. S. Fan, "Analysis of Flow in Gas-Liquid Bubble Columns Using Multi-Resolution Methods," *Trans. Inst. Chem. Eng.*, **33**(Part A), 608 (1995).

Bai, D., A. S. Issangya, and J. R. Grace, "Characteristic of Gas-Fluidized Beds in Different Flow Regimes," *Ind. Eng. Chem. Res.*, **38**, 803 (1999).

Bai, D., E. Shibuya, N. Nakagawa, and K. Kato, "Fractal Characteristics of Gas-Solids Flow in a Circulating Fluidized Bed," *Powder Technol.*, **90**, 205 (1997a).

Bai, D., H. T. Bi, and J. R. Grace, "Chaotic Behavior of Fluidized Beds Based on Pressure and Voidage Fluctuations," *AIChE J.*, **43**, 1357 (1997b).

Bai, D., E. Shibuya, Y. Masuda, N. Nakagawa, and K. Kato, "Flow Structure in a Fast Fluidized Bed," *Chem. Eng. Sci.*, **51**, 957 (1996).

Bi, H. T., J. R. Grace, and J. X. Zhu, "Propagation of Pressure Waves and Forced Oscillation of Fluidized Beds and their Effects on Measurements of Local Hydrodynamics," *Powder Technol.*, **82**, 239 (1995).

Briens, C. L., L. A. Briens, J. Hay, C. Hudson, and A. Margaritis, "Hurst's Analysis to Detect Minimum Fluidization and Gas Maldistribution in Fluidized Beds," *AIChE J.*, **43**, 1904 (1997).

Cabrejos, F. J., and G. E. Klinzing, "Characterization of Dilute Flows Using the Rescaled Range Analysis," *Powder Technol.*, **84**, 139 (1995).

Cassanello, M., F. Larachi, M. N. Marie, C. Guy, and J. Chaouki, "Experimental Characterization of the Solid Phase Chaotic Dynamics in Three-Phase Fluidization," *Ind. Eng. Chem. Res.*, **34**, 2971 (1995).

Cohen, A., and I. Procaccia, "Computing the Kolmogorov Entropy from Time Signals of Dissipative and Conservative Dynamical Systems," *Phys. Rev. A*, **31**, 1872 (1985).

Cui, H., J. Li, M. Kwauk, H. An, M. Chen, Z. Ma, and G. Wu, "Dynamic Behaviors of Heterogeneous Flow Structure in Gas-Solid Fluidization," *Powder Technol.*, **112**, 7 (2000).

Daubechies, I., "Orthonormal Bases of Compactly Supported Wavelets," *Commun. Pure Appl. Math.*, **41**, 909 (1988).

Daw, C. S., and J. S. Halow, "Evaluation and Control of Fluidization Quality Through Chaotic Time Series Analysis of Pressure Drop Measurements," *AIChE Symp. Ser.*, **89**(296), 103 (1993).

Daw, C. S., C. E. A. Finney, M. Vasudevan, N. A. Van Goor, K. Nguyer, D. D. Bruns, E. J. Kostelich, C. Grebogi, E. Ott, and J. A. Yorke, "Self Organization and Chaos in a Fluidized Bed," *Phys. Rev. Lett.*, **75**, 2308 (1995).

Daw, C. S., W. F. Lawkins, D. J. Downing, and N. E. Clapp, Jr., "Chaotic Characteristics of a Complex Gas-Solid Flow," *Phys. Rev. A*, **41**, 1179 (1990).

Drahos, J., F. Bradka, and M. Puncochar, "Fractal Behaviour of Pressure Fluctuations in a Bubble Column," *Chem. Eng. Sci.*, **47**, 4069 (1992).

Fan, L. T., D. Neogi, M. Yashima, and R. Nassar, "Stochastic Analysis of a Three-Phase Fluidized Bed: Fractal Approach," *AIChE J.*, **36**, 1529 (1990).

Fan, L. T., T. C. Ho, S. Hiraoka, and W. P. Walawender, "Pressure Fluctuation in a Fluidized Bed," *AIChE J.*, **27**, 388 (1981).

Fan, L. T., Y. Kang, D. Neogi, and M. Yashima, "Fractal Analysis of Fluidized Particle Behavior in Liquid-Solid Fluidized Beds," *AIChE J.*, **39**, 513 (1993).

Franca, F., M. Acikgoz, R. T. Lahey, Jr., and A. Clausse, "The Use of Fractal Techniques for Flow Regime Identification," *Int. J. Multiphase Flow*, **17**, 545 (1991).

Göz, M. F., "Nonlinear Waves in Two-Fluid Flows," *Physica D*, **123**, 112 (1998).

Grassberger, P., and I. Procaccia, "Characterization of Strange Attractors," *Phys. Rev. Lett.*, **50**, 346 (1983a).

Grassberger, P., and I. Procaccia, "Estimation of the Kolmogorov Entropy from a Chaotic Signal," *Phys. Rev. A*, **28**, 2591 (1983b).

Guo, Q., G., Yue, and J. Werther, "Dynamics of Pressure Fluctuation in a Bubbling Fluidized Bed at High Temperature," *Ind. Eng. Chem. Res.*, **41**, 3482 (2002).

Harris, S. E., and D. G. Crighton, "Solitons, Solitary Waves, and Voidage Disturbances in Gas-Fluidized Beds," *J. Fluid Mech.*, **266**, 243 (1994).

He, Z., W. Zhang, K. He, and B. Chen, "Modeling Pressure Fluctuations via Correlation Structure in a Gas-Solids Fluidized Bed," *AIChE J.*, **43**, 1919 (1997).

Hurst, H. E., "Long-Term Storage Capacity of Reservoirs," *Trans. Amer. Soc. Civil Engs.*, **116**, 770 (1951).

Ji, H., H. Ohara, K. Kuramoto, A. Tsutsumi, K. Yoshida, and T. Hirama, "Nonlinear Dynamics of Gas-Solid Circulating Fluidized-Bed System," *Chem. Eng. Sci.*, **55**, 403 (2000).

Johnsson, F., R. C. Zijerveld, J. C. Schouten, C. M. van den Bleek, and B. Leckner, "Characterization of Fluidization Regimes by Time-Series Analysis of Pressure Fluctuations," *Int. J. Multiphase Flow*, **26**, 663 (2000).

Karamavruc, A. I., and N. N. Clark, "A Fractal Approach for Interpretation of Local Instantaneous Temperature Signals around a Horizontal Heat Transfer Tube in a Bubbling Fluidized Bed," *Powder Technol.*, **90**, 235 (1997a).

Karamavruc, A. I., and N. N. Clark, "Local Differential Pressure Analysis in a Slugging Bed Using Deterministic Time-Delay Embedding Theory," *Chem. Eng. Sci.*, **52**, 357 (1997b).

Karamavruc, A. I., N. N. Clark, and J. S. Halow, "Application of Mutual Information Theory to Fluid Bed Temperature and Differential Pressure Signal Analysis," *Powder Technol.*, **84**, 247 (1995).

Kikuchi, R., A. Tsutsumi, and K. Yoshida, "Fractal Aspect of Hydrodynamics in a Three-Phase Fluidized Bed," *Chem. Eng. Sci.*, **51**, 2865 (1996).

Komatsu, T. S., and H. Hayakawa, "Nonlinear Waves in Fluidized Beds," *Phys. Lett. A*, **183**, 56 (1993).

Kozma, R., H. Kok, M. Sakuma, D. D. Djainal, and M. Kitamura, "Characterization of Two-Phase Flows Using Fractal Analysis of Local Temperature Fluctuations," *Int. J. Multiphase Flow*, **22**, 953 (1996).

Li, H., "Application of Wavelet Multi-resolution Analysis to Pressure Fluctuations of Gas−Solid Two-Phase Flow in a Horizontal Pipe," *Powder Technol.*, **125**, 61 (2002).

Li, J., "Compromise and Resolution—Exploring the Multi-Scale Nature of Gas-Solid Fluidization," *Powder Technol.*, **111**, 50 (2000).

Li, J., and M. Kwauk, "Multi-Scale Methodology for Process Engineering," *Prog. Nat. Sci.*, **9**, 1073 (1999).

Li, J., and M. Kwauk, *Particle-Fluid Two-Phase Flow—The Energy-Minimization Multi-Scale Method*, Metallurgical Industry Press, Beijing (1994).

Li, J., C. Chen, Z. Zhang, J. Yuan, A. Nemet, and F. N. Fett, "The EMMS Model—Its Application, Development and Updated Concepts," *Chem. Eng. Sci.*, **54**, 5409 (1999).

Li, J., L. Wen, G. Qian, H. Cui, and M. Kwauk, "Structure Heterogeneity, Regime Multiplicity and Nonlinear Behavior in Particle-Fluid Systems," *Chem. Eng. Sci.*, **51**, 2693 (1996).

Lu, X., and H. Li, "Wavelet Analysis of Pressure Fluctuation Signals in a Bubbling Fluidized Bed," *Chem. Eng. J.*, **75**, 113 (1999).

Mallat, S. G., "A Theory for Multiresolution Signal Decomposition: The Wavelet Representation," *IEEE Trans. Pattern Anal. Mach. Intell.*, **11**, 674 (1989).

Mandelbrot, B. B., and J. W. Van Ness, "Fractional Brownian Motions, Fractional Noises and Applications," *SIAM Rev.*, **10**, 422 (1968).

Marzocchella, A., R. C. Zijerveld, J. C. Schouten, and C. M. van den Bleek, "Chaotic Behavior of Gas-Solids Flow in the Riser of a Laboratory-Scale Circulating Fluidized Bed," *AIChE J.*, **43**, 1458 (1997).

Mauuci, E., C. L. Briens, R. J. Martinuzzi, and D. Wild, "Detection and Characterization of Piston Flow Regime in Three-Phase Fluidized Beds," *Powder Technol.*, **103**, 243 (1999).

Qi, G., "Wavelet-Based AE Characterization of Composite Materials," *NDT & Int.*, **33**, 133 (2000).

Ren, J., Q. Mao, J. Li, and W. Lin, "Wavelet Analysis of Dynamic Behavior in Fluidized Beds," *Chem. Eng. Sci.*, **56**, 981 (2001).

Rioul, O., and P. Duhamel, "Fast Algorithms for Discrete and Continuous Wavelet Transforms," *IEEE Trans. Inf. Theory*, **38**, 569 (1992).

Schouten, J. C., and C. M. van den Bleek, "Monitoring the Quality of Fluidization Using the Short-Term Predictability of Pressure Fluctuations," *AIChE J.*, **44**, 48 (1998).

Schouten, J. C., M. L. M. vander Stappen, and C. M. Van den Bleek, "Scale up of Chaotic Fluidized Bed Hydrodynamics," *Chem. Eng. Sci.*, **51**, 1991 (1996).

Schouten, J. C., R. C. Zijerveld, and C. M. van den Bleek, "Scale-Up of Bottom-Bed Dynamics and Axial Solids-Distribution in Circulating Fluidized Beds of Geldart-B Particles," *Chem. Eng. Sci.*, **54**, 2103 (1999).

Tewfik, A. H., D. Sinha, and P. Jorgensen, "On the Optimal Choice of a Wavelet for Signal Representation," *IEEE Trans. Inf. Theory*, **38**, 747 (1992).

Tsonis, A. A., *Chaos from Theory to Applications*, Plenum Press, New York (1992).

Van den Bleek, C. M., and J. C. Schouten, "Can Deterministic Chaos Create Order in Fluidized Bed Scale-Up?," *Chem. Eng. Sci.*, **48**, 2367 (1993a).

Van den Bleek, C. M., and J. C. Schouten, "Deterministic Chaos: A New Tool in Fluidized Bed Design and Operation," *Chem. Eng. J.*, **53**, 75 (1993b).

Van der Schaaf, J., J. C. Schouten, and C. M. van den Bleek, "Origin, Propagation and Attenuation of Pressure Waves in Gas-Solid Fluidized Beds," *Powder Technol.*, **95**, 220 (1998).

Zhao, G. B., J. Z. Chen, and Y. R. Yang, "Predictive Model and Deterministic Mechanism in a Bubbling Fluidized Bed," *AIChE J.*, **47**, 1524 (2001a).

Zhao, G. B., Y. F. Shi, G. Q. Guan, and H. R. Yu, "Chaotic Method for Distinguishing Between Particulate and Aggregative Fluidization," *Proc. Fluidization X*, Beijing, P. R. China, p. 157 (2001b).

Zhao, G. B., L. L. Gu, Y. F. Shi, and H. R. Yu, "Distinguishing between Particulate and Aggregative Fluidization Using Chaos Theory," *J. Chem. Ind. Eng. (China)*, **51**, 468 (2000).

Zhao, G. B., Y. F. Shi, W. F. Duan, and H. R. Yu, "Computing Fractal Dimension and the Kolmogorov Entropy from Chaotic Time Series," *Chin. J. Comput. Phys.*, **16**, 309 (1999).

Zijerveld, R. C., F. Johnsson, A. Marzocchella, J. C. Schouten, and C. M. van den Bleek, "Fluidization Regimes and Transitions from Fixed Bed to Dilute Transport Flow," *Powder Technol.*, **95**, 185 (1998).

Manuscript received May 21, 2002, and revision received Oct. 8, 2002.